











Parallel flows as a key component to interpret Super-X divertor experiments

M. Carpita^{*} , O. Février , H. Reimerdes , C. Theiler , B.P. Duval, C. Colandrea, G. Durr-Legoupil-Nicoud, D. Galassi , S. Gorno , E. Huett, J. Loizu, L. Martinelli, A. Perek , L. Simons, G. Sun , E. Tonello , C. Wüthrich  and the TCV Team^a

EPFL-SPC, CH-1015 Lausanne, Switzerland

E-mail: massimo.carpita@epfl.ch

Received 6 October 2023, revised 5 February 2024

Accepted for publication 16 February 2024

Published 28 February 2024



Abstract

The Super-X Divertor (SXD) is an alternative divertor configuration leveraging total flux expansion at the Outer Strike Point (OSP). While the *extended 2-Point Model* (2PM) predicts facilitated detachment access and control in the SXD configuration, these attractive features are not always retrieved experimentally. These discrepancies are at least partially explained by the effect of parallel flows which, when self-consistently included in the 2PM, reveal the role of total flux expansion on the pressure balance and weaken the total flux expansion effect on detachment access and control, compared to the original predictions. This new model can partially explain the discrepancies between the 2PM and experiments performed on tokamak à configuration variable (TCV), in ohmic L-mode scenarios, which are particularly apparent when scanning the OSP major radius R_t . In core density ramps in lower Single-Null (SN) configuration, the impact of R_t on the CIII emission front movement in the divertor outer leg—used as a proxy for the plasma temperature in the divertor—is substantially weaker than 2PM predictions. Furthermore, in OSP radial sweeps in lower and upper SN configurations, in ohmic L-mode scenarios with a constant core density, the peak parallel particle flux density at the OSP is almost independent of R_t , while the 2PM predicts a linear dependence. Finally, analytical and numerical modeling of parallel flows in the divertor is presented. It is shown that an increase in total flux expansion can favour supersonic flows at the OSP. Parallel flows are also shown to be relevant by analysing SOLPS-ITER simulations of TCV.

Keywords: power exhaust, divertor, detachment, total flux expansion, mach number, parallel flows

(Some figures may appear in colour only in the online journal)

^a See Reimerdes *et al* 2022 (<https://doi.org/10.1088/1741-4326/ac369b>) for the TCV Team.

^{*} Author to whom any correspondence should be addressed.



Original Content from this work may be used under the terms of the [Creative Commons Attribution 4.0 licence](https://creativecommons.org/licenses/by/4.0/). Any further distribution of this work must maintain attribution to the author(s) and the title of the work, journal citation and DOI.

1. Introduction

Power exhaust is a key challenge for the realization of a magnetic confinement fusion reactor, based on the tokamak concept, as identified by the European roadmap for fusion energy [1]. In a future power plant, large power losses from the confined plasma must be exhausted in a very narrow Scrape-Off-Layer (SOL) region. The peak power density at the target, if unmitigated, is predicted to greatly exceed material limits [2]. Moreover, avoiding excessive long-term erosion on the reactor vessel components requires a sufficiently low plasma target temperature [3].

Diverted plasma configurations are employed for power exhaust, with the ability to support a large plasma temperature gradient between the confined plasma and the divertor targets. At sufficiently low electron temperature T_e , radiation by hydrogen and low-Z impurities becomes more efficient ($T_e \lesssim 10$ eV), and the cross-sections for charge exchange ($T_i \lesssim 5$ eV) and volumetric recombination ($T_e \lesssim 1$ eV) increase, transferring some of the plasma momentum and energy to neutrals [4, 5] and redistributing the exhausted power more isotropically on the plasma facing components. This greatly reduces the peak power and particle fluxes to the targets and allows operation in the *detached* regime.

The Lower-Single-Null (LSN) is currently the reference configuration for most operating tokamaks and is the chosen configuration for ITER [6]. Nonetheless, the extrapolation of this configuration to future reactors, with higher power and particle fluxes, cannot be safely assumed. Alternative Divertor Configurations (ADCs) are, therefore, studied as potential solutions to this problem. ADCs' promised benefits include easier access to detachment and better control over the location of the radiation front [7]. Such predictions, and their extrapolation to future reactors, must be confirmed by experiments and understood through comprehensive modeling [8].

Among ADCs, one considered concept for future reactors is the Super-X Divertor (SXD) [9]. Its main feature is an increase of the Outer Strike Point (OSP) major radius R_t , which comes with an increased total flux expansion. The increase of R_t increases the cross-sectional area of a flux tube $A_{\perp,t}$ (as the total magnetic field B_{tot} is proportional to the inverse of the major radius R^{-1}) and, as a result, decreases the parallel power densities at the target, $q_{\parallel,t}$. For a constant grazing angle at the outer target, an increase in R_t results in a linear increase of the target wetted area and a R_t^{-1} decrease of the power density at the OSP. This predicted dependency of the power density has been confirmed experimentally [7]. According to the *extended 2-Point Model* (2PM) [10, 11], the key advantages of the SXD are facilitated detachment access and control. However, these predictions were neither consistently retrieved experimentally [7, 12, 13] nor numerically [14]. Possible arguments for this disagreement included target geometry [12], neutral compression [15, 16], and/or the divertor being in a sheath-limited regime [14]. However, a general understanding of the discrepancy is still pending.

This paper discusses the role of R_t for both target conditions and detachment access and control. Section 2 presents the 2PM, its predictions with respect to total flux expansion

effects on detachment access and control, and its modification to reveal the effect of parallel flows on the total pressure balance, leading to predictions of weaker total flux expansion effects compared to the original ones. Section 3 presents SXD experiments on the tokamak à configuration variable (TCV) tokamak [13] to investigate the role of R_t . Finally, in section 4, the analytical and numerical modeling of parallel flows in the divertor is presented, showing that an increase in total flux expansion can favor supersonic flows at the OSP and that parallel flows are relevant by analyzing SOLPS-ITER [17] simulations of TCV. A summary and conclusions are presented in section 5.

2. 2PM extension accounting for parallel flows

The 2PM [10, 18] is a reduced model that relates target quantities (electron temperature $T_{e,t}$, electron density $n_{e,t}$, parallel particle flux density Γ_t) with upstream parameters for the SOL plasma (total plasma pressure $p_{tot,u}$ and parallel power density $q_{\parallel,u}$). These quantities pertain to one individual flux tube in the SOL and are linked together by momentum and power balances. The upstream location, labeled u , is somewhat arbitrary and can refer to the X-point location, the outer mid-plane (OMP), etc. It is usually taken as the stagnation point where $v_{\parallel} = 0$. In the following, this location will be specified when needed.

In the 2PM, the parallel power density q_{\parallel} is defined as the total parallel plasma power density, assuming $n_e = n_i = n$ and $T_e = T_i = T$ (here and in the following T is referred to in energy units)

$$q_{\parallel} = q_{\parallel}^{\text{conv}} + q_{\parallel}^{\text{cond}} \quad (1)$$

with $q_{\parallel}^{\text{conv}} = (5nT + \frac{1}{2}m_i n v_{\parallel}^2)v_{\parallel}$ being the parallel convected power density, $q_{\parallel}^{\text{cond}}$ being the parallel conducted power density, and v_{\parallel} the parallel plasma velocity.

2.1. 2PM predictions for target quantities and their dependence on R_t

The most general 2PM expressions for target quantities are reported by Stangeby in (15)–(17) of [10]. These are equivalent to expressions obtained by Kotov and Reiter in [19] that were derived from the steady-state version of the equations solved by the 2D multi-species plasma fluid code B2.

These expressions are reported here, assuming the following simplifying hypotheses: (S-I) only hydrogenic ion species (i.e. $n = n_e = n_i$) and no net current (i.e. $v_{\parallel} = v_{e,\parallel} = v_{i,\parallel}$); (S-II) thermal equilibration along the flux tube (i.e. $T = T_e = T_i$); (S-III) a sonic plasma flow at the target (i.e. $M_t = 1$, where $M = v_{\parallel}/c_s$ is the Mach number and $c_s = \sqrt{(T_e + T_i)/m_i} = \sqrt{2T/m_i}$ the sound speed¹, and the subscript t representing the target in what follows). Hypothesis (S-III) and its link to

¹ Here and in the following the *isothermal sound speed* $c_s = \sqrt{(T_e + T_i)/m_i}$ is referred to as *sound speed* for simplicity. The same applies for the *Mach number* defined through c_s .

the total flux expansion effects are discussed in section 4.1. These assumptions, introduced for simplicity, can be easily relaxed and do not limit the following discussion. An additional assumption *required* in the derivation of the following 2PM expressions is: (A-I) target quantities are evaluated at the sheath entrance (i.e. $q_{||,t} = q_{||,se} = \gamma n_t T_t c_{s,t}$, where γ is the sheath heat transmission coefficient [18]). Further details are provided in appendix A. The expressions are

$$T_t^{2PM} = \frac{8m_i}{\gamma^2} \cdot \frac{q_{||,u}^2}{p_{tot,u}^2} \cdot \frac{(1-f_{cooling})^2}{(1-f_{mom-loss})^2} \cdot \left(\frac{R_u}{R_t}\right)^2 \quad (2)$$

$$n_t^{2PM} = \frac{\gamma^2}{32m_i} \cdot \frac{p_{tot,u}^3}{q_{||,u}^2} \cdot \frac{(1-f_{mom-loss})^3}{(1-f_{cooling})^2} \cdot \left(\frac{R_u}{R_t}\right)^{-2} \quad (3)$$

$$\Gamma_t^{2PM} = \frac{\gamma}{8m_i} \cdot \frac{p_{tot,u}^2}{q_{||,u}} \cdot \frac{(1-f_{mom-loss})^2}{(1-f_{cooling})} \cdot \left(\frac{R_u}{R_t}\right)^{-1} \quad (4)$$

where $R_{u/t}$ are the upstream and target major radii respectively. The power and momentum loss factors, $f_{cooling}$ and $f_{mom-loss}$, are

$$\frac{q_{||,t}}{q_{||,u}} \cdot \frac{R_t}{R_u} \equiv 1 - f_{cooling} \quad (5)$$

$$\frac{p_{tot,t}}{p_{tot,u}} \equiv 1 - f_{mom-loss} \quad (6)$$

and the total plasma pressure is

$$p_{tot} = 2nT + m_i n v_{||}^2 = 2(1 + M^2)nT. \quad (7)$$

The ratio (R_u/R_t) in (2)–(4) explicitly relates target quantities to total flux expansion. Both, experiments and simulations [7, 12, 14], were performed to test these dependencies of target quantities on R_t , showing several discrepancies.

2.2. Explicit dependence of $f_{mom-loss}$ on R_t and the effective Mach number M_{eff}

The loss factors $f_{cooling}$ and $f_{mom-loss}$ are parameters accounting for a variety of complex physical processes [12, 14–16]. These processes can be separated into two main groups: (1) volumetric sources and sinks, and cross-field transport effects; (2) geometrical effects, related to flux tube cross-sections. This work focuses mainly on the latter, as they can be explicitly linked to total flux expansion effects, as shown in the following.

While $f_{cooling}$ relates only to processes pertaining to group (1), $f_{mom-loss}$ also accounts for geometrical effects. To show this, the steady-state local power and parallel momentum balances in a flux tube element are taken

$$\frac{1}{A_{\perp}} \partial_s (A_{\perp} q_{||}) = S_{pwr} \quad (8)$$

$$\frac{1}{A_{\perp}} \partial_s (A_{\perp} m_i n v_{||}^2) = -\partial_s (2nT) + S_{mom} \quad (9)$$

where s is a length coordinate along the flux tube and $S_{pwr/mom}$ are effective sources (or sinks) within the flux tube, respectively for power and momentum, related to processes pertaining to group (1). As in a flux tube $A_{\perp} \propto B_{tot}^{-1} \propto R$, rearranging (8) and (9) yields

$$\frac{1}{q_{||}} \partial_s (q_{||}) = \frac{S_{pwr}}{q_{||}} - \frac{1}{R} \partial_s (R) \quad (10)$$

$$\frac{1}{p_{tot}} \partial_s (p_{tot}) = \frac{S_{mom}}{p_{tot}} - \frac{\kappa}{R} \partial_s (R) \quad (11)$$

where $\kappa = m_i n v_{||}^2 / p_{tot} = M^2 / (1 + M^2)$ is the local ratio of dynamic and total pressure in the flux tube. Integrating (10) and (11) from upstream to target, rearranging, and using (5) and (6) yields

$$\frac{q_{||,t}}{q_{||,u}} \cdot \frac{R_t}{R_u} = \exp \left(\int_u^t \frac{S_{pwr}}{q_{||}} ds \right) \equiv 1 - f_{cooling} \quad (12)$$

$$\frac{p_{tot,t}}{p_{tot,u}} = \exp \left(\int_u^t \left[\frac{S_{mom}}{p_{tot}} - \frac{\kappa}{R} \partial_s (R) \right] ds \right) \equiv 1 - f_{mom-loss}. \quad (13)$$

It thus becomes apparent that $f_{mom-loss}$ includes geometrical effects, whereas $f_{cooling}$ does not. In literature, the influence of geometrical effects on $f_{mom-loss}$ was recognized, but not investigated in detail, as it was considered negligible or avoided for simplicity [10, 14].

To explicitly highlight the effect of total flux expansion on the total pressure variation, it is useful to rewrite (13) in a form similar to (12). A constant κ_{eff} is introduced, which satisfies

$$\int_u^t \frac{\kappa}{R} \partial_s (R) ds = \kappa_{eff} \int_u^t \frac{1}{R} \partial_s (R) ds \quad (14)$$

κ_{eff} is then the average of the ratio of dynamic to total pressure, weighted by the local relative variation of the flux tube area, between upstream and target. (13) then becomes

$$1 - f_{mom-loss} \equiv \frac{p_{tot,t}}{p_{tot,u}} = \left(\frac{R_u}{R_t} \right)^{\kappa_{eff}} \exp \left(\int_u^t \frac{S_{mom}}{p_{tot}} ds \right). \quad (15)$$

This equation now explicitly shows the effect of total flux expansion on the total pressure variation. It also reveals the explicit dependence of $f_{mom-loss}$ on total flux expansion.

An additional quantity can be defined to substitute κ_{eff} in (15), termed the effective Mach number M_{eff}

$$M_{eff} = \sqrt{\frac{\kappa_{eff}}{1 - \kappa_{eff}}} \leftrightarrow \kappa_{eff} = \frac{M_{eff}^2}{1 + M_{eff}^2} \quad (16)$$

From here, M_{eff} will be used. Further insights on κ_{eff} and M_{eff} , and their physical interpretation, are provided in appendix B.

2.3. Consequence on target quantities scaling

The result obtained in (15) is now considered together with (2)–(4). For the sake of clarity, the following notation is introduced

$$1 - f_{\text{cooling}} \equiv (1 - f_{\text{cooling}}^S) \quad (17)$$

$$1 - f_{\text{mom-loss}} \equiv (1 - f_{\text{mom-loss}}^S) \cdot \left(\frac{R_u}{R_t} \right)^{\frac{M_{\text{eff}}^2}{1+M_{\text{eff}}^2}} \quad (18)$$

The newly defined factors f_{cooling}^S and $f_{\text{mom-loss}}^S$ account for the same physics, i.e. volumetric sources and cross-field effects only. With this new definition of loss factors, (2)–(4) become

$$T_t^{\text{mod}} = \frac{8m_i}{\gamma^2} \cdot \frac{q_{\parallel,u}^2}{p_{\text{tot},u}^2} \cdot \frac{(1 - f_{\text{cooling}}^S)^2}{(1 - f_{\text{mom-loss}}^S)^2} \cdot \left(\frac{R_u}{R_t} \right)^{2 - \frac{2M_{\text{eff}}^2}{1+M_{\text{eff}}^2}} \quad (19)$$

$$n_t^{\text{mod}} = \frac{\gamma^2}{32m_i} \cdot \frac{p_{\text{tot},u}^3}{q_{\parallel,u}^2} \cdot \frac{(1 - f_{\text{mom-loss}}^S)^3}{(1 - f_{\text{cooling}}^S)^2} \cdot \left(\frac{R_u}{R_t} \right)^{-2 + \frac{3M_{\text{eff}}^2}{1+M_{\text{eff}}^2}} \quad (20)$$

$$\Gamma_t^{\text{mod}} = \frac{\gamma}{8m_i} \cdot \frac{p_{\text{tot},u}^2}{q_{\parallel,u}} \cdot \frac{(1 - f_{\text{mom-loss}}^S)^2}{(1 - f_{\text{cooling}}^S)} \cdot \left(\frac{R_u}{R_t} \right)^{-1 + \frac{2M_{\text{eff}}^2}{1+M_{\text{eff}}^2}} \quad (21)$$

The dependence of target quantities on R_u/R_t now varies with M_{eff} , figure 1, and is generally weakened with increasing M_{eff} . The qualitative dependence of Γ_t^{mod} and n_t^{mod} on $1/R_t$ even reverses for $M_{\text{eff}} \geq 1$ and $\geq \sqrt{2}$, respectively. When $M_{\text{eff}} = 0$, the dependence of target quantities on R_u/R_t recovers the original ones, (2)–(4).

2.4. Consequence on detachment window

It has been predicted that the Super-X configuration increases detachment front stability and facilitates detachment control [8, 11, 20], due to a larger control parameter range for detached operation with tolerable consequences for core performance. This is a consequence of the negative parallel power density gradient that total flux expansion establishes towards the target, which opposes the movement of the radiation front. In terms of the operational window for detachment, Lipschultz *et al* (see (30) of [11]) provided an analytical estimate for the dependence of the detachment window on $B_{\text{tot}} \propto R_t^{-1}$

$$\frac{\zeta_x}{\zeta_t} = \left[\frac{R_t}{R_x} \right]^\beta \quad (22)$$

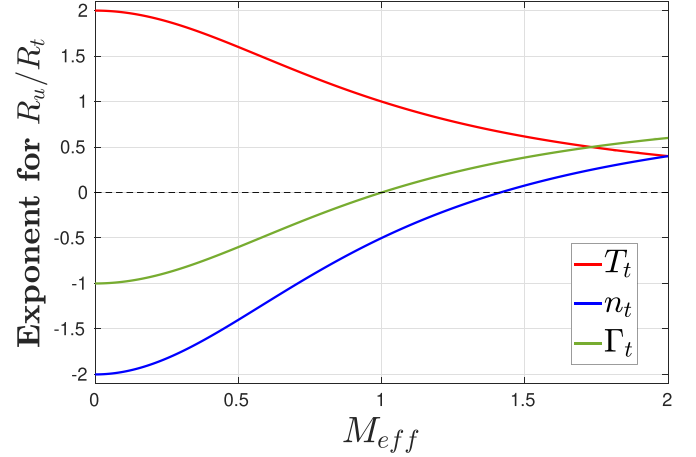


Figure 1. Exponents of R_u/R_t for target temperature T_t^{mod} (red), target density n_t^{mod} (blue) and parallel particle flux density Γ_t^{mod} (green), plotted against the effective Mach number M_{eff} .

where $\zeta_{x,t}$ are the values of a control parameter $\zeta = [p_u, f_i, P_{\text{SOL}}]$, that correspond to the detachment front² being at the X-point or at the target, respectively. The three control parameters considered in this work are the upstream static pressure $p_u = 2n_u T_u$ (instead of n_u , as used in [11]), the impurity fraction f_i and the power entering the SOL in the flux tube of interest P_{SOL} . $R_{x,t}$ are the X-point and the target major radii, respectively. $\beta = [1, 2, -1]$ is a specific exponent related to the considered control parameter. The differences between (22) of this work and (30) of [11], and the values for the exponent β , are a consequence of keeping p_u as a control parameter instead of n_u , and identifying the upstream location with the X-point (see appendix B).

The derivation of (22) uses a momentum balance equivalent to the one in the 2PM and does not explicitly account for any p_u variation from upstream to target, i.e. flux expansion effects and/or total pressure redistribution between dynamic and static contributions. When taken into account, the dependence of the detachment window on $B_{\text{tot}} \propto R_t^{-1}$ becomes

$$\frac{\zeta_x}{\zeta_t} = \left[\left(\frac{R_t}{R_x} \right)^{1 - \frac{M_{\text{eff}}^2}{1+M_{\text{eff}}^2}} \cdot \frac{1 + M_x^2}{1 + M_t^2} \right]^\beta \quad (23)$$

where the first factor in (23) accounts for the total flux expansion, and the second factor accounts for the total pressure redistribution between dynamic and static contributions. Further details on the derivation of (23) are provided in appendix C. The inclusion of total flux expansion and redistribution effects on total pressure reveals that the static pressure p can include a gradient towards the target. In particular, p is proportional to the radiated power in the detachment front, as shown in (C.8). Consequentially, a negative gradient

² The detachment front is intended here as the location where, ideally, all of the power loss occurs in a flux tube [11, 20], separating a hot, attached upstream portion of the flux tube and a cold, detached downstream portion in front of the target.

of the static pressure, as opposed to parallel power density, provides positive feedback for the upstream movement of the detachment front and, hence, weakens the total flux expansion dependence of the detachment window.

2.5. Summary of the effects of parallel flows on total flux expansion

The importance of including total flux expansion in the momentum balance was shown, and the following important points were highlighted:

- The total pressure variation along a flux tube, see (15), can be linked explicitly to total flux expansion via M_{eff} , a parameter characterizing flows in the flux tube of interest.
- Increasing M_{eff} generally weakens the dependence on R_t of target quantities, see (19)–(21), and detachment window, see (23), compared to predictions by the 2PM. In the case of ‘effective supersonic’ flows ($M_{\text{eff}} \geq 1$), the dependencies of target density and particle flux on R_t can even reverse.
- M_{eff} depends on both the flow patterns in the flux tube and the geometrical design of the leg, in particular on the change of relative flux expansion along field lines, i.e. $R^{-1} \partial_s(R)$, see (14) and (16). Two different divertor geometries, characterized by the same flow patterns and total flux expansion, can exhibit different behavior with respect to their sensitivity to R_t , discussed in detail in appendix B.

3. SXD experiments in TCV and comparison with 2PM predictions

Experiments to investigate the SXD configuration are carried out in the *Tokamak à Configuration Variable* (TCV) [13, 21], testing the 2PM predictions presented in section 2.1, regarding total flux expansion effects on detachment access and control. TCV is a medium-sized tokamak ($R_0 \sim 0.88$ m, $B_0 < 1.45$ T, $a \sim 0.25$ m) with a highly elongated open vessel and 16 independently-powered poloidal field coils, allowing for unique shaping capabilities. The almost complete coverage of the vessel surfaces with graphite tiles allows for flexible placement of particle and power loads.

3.1. Key diagnostics and experimental approach

Different plasma geometries, characterized by varying OSP major radius R_t , are employed in this study, figure 2. A set of polycrystalline graphite tiles, characterized by a longer structure on the low-field side compared to the high-field side (SILO baffles), is also employed in some experiments. They are designed to increase divertor closure, whilst maintaining good compatibility with ADCs [22, 23].

Gas valves at the floor, the Inner Wall (IW) and the ceiling of the vessel, figure 2(b), can be used for D_2 fuelling, allowing to test the possible impact of fuelling locations on

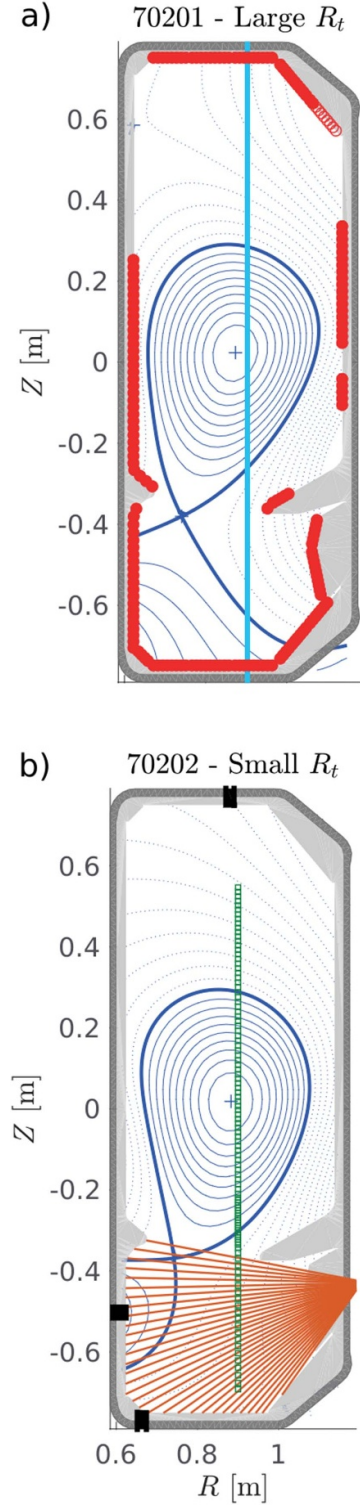


Figure 2. Examples of baffled geometries used in the experimental work (large and small R_t). (a) The red dots indicate the position of wall-embedded Langmuir probes, while the cyan line indicates the FIR chord used for the feedback control of fuelling. (b) The black rectangles indicate the poloidal location of fuelling valves, the orange lines indicate the lines of sight of the DSS and the green dots indicate Thomson scattering measurement locations (intercepts between the laser and spectrometer lines of sight).

the experiments. The flow rates are feedback controlled and can be adjusted according to the line-integrated density n_{int} measurements by a Far-Infrared (FIR) interferometer, along a vertical chord, figure 2(a). Density and temperature measurements in the core and across the separatrix are obtained by Thomson scattering [24], figure 2(b). The local TS density measurements are then post-processed to evaluate the line-averaged core density $\langle n_e \rangle$. Wall-embedded Langmuir Probes (LP) [25] cover a large part of the poloidal perimeter of the vessel, figure 2(a). These were operated with a triangular voltage sweep (from -120 to 80 V at ~ 330 Hz and ~ 990 Hz frequencies), in order to obtain temperature measurements as well as particle flux. Details on their analyses are provided in [26]. Line radiation and their distributions are obtained from a Divertor Spectroscopy System (DSS) [27] and from a system of filtered optical cameras, MANTIS [28], that provide 2D poloidal map inversions of the emissivity for selected radiating spectral lines. This work focuses, in particular, on the CIII (465.8 nm) line emission to obtain emissivity profiles. In previous TCV studies, the CIII radiation front along a divertor leg (determined as the location where the emissivity profile along the outer leg drops by 50% with respect to the peak) was shown to provide a convenient estimation of the detachment status of the divertor. Due to a strong dependency on the local electron temperature, the CIII radiation front is a reliable proxy to identify the low temperature region along the outer leg [23, 29]. A system of 64 gold foil bolometers, then substituted with a new system of 120 channels [30], is used to obtain radiation emissivity maps across a TCV poloidal section by tomographically inverting their line integrated chord intensities. The Grad-Shafranov solver LIUQE [31] is used to reconstruct the equilibria.

Two different scenarios are explored in this work, both with a plasma current $I_p \sim 250$ kA and the ion ∇B drift directed from the X-point towards the core, to avoid H-mode [7]. The first employs ohmically-heated L-mode core density ramps $\langle n_e \rangle \simeq [4.0 \rightarrow 10.0] \cdot 10^{19} \text{ m}^{-3}$ (corresponding to $f_g \simeq [0.20 \rightarrow 0.55]$, f_g being the Greenwald fraction). The density ramp is performed separately for two LSN configurations with small and large R_t , respectively. SILO baffles are employed to increase divertor closure, which is expected to improve the match between the 2PM predictions and experimental results, according to SOLPS-ITER simulations of TCV [15]. Fuelling is performed from either the floor, IW or ceiling valves. The second scenario employs ohmically-heated L-mode OSP target radius R_t scans at constant density $\langle n_e \rangle \simeq 5.5 \cdot 10^{19} \text{ m}^{-3}$ ($f_g \simeq 0.31$). This scenario is repeated in both LSN or Upper-Single-Null (USN) configurations, with either SILO baffles or without, and floor-only fuelling.

3.2. Density ramps at constant R_t

Two values of R_t are investigated during core density ramps: $R_t \simeq 0.62$ m (small R_t) and $R_t \simeq 1.03$ m (large R_t). When ramping the core density, the temperature in the divertor

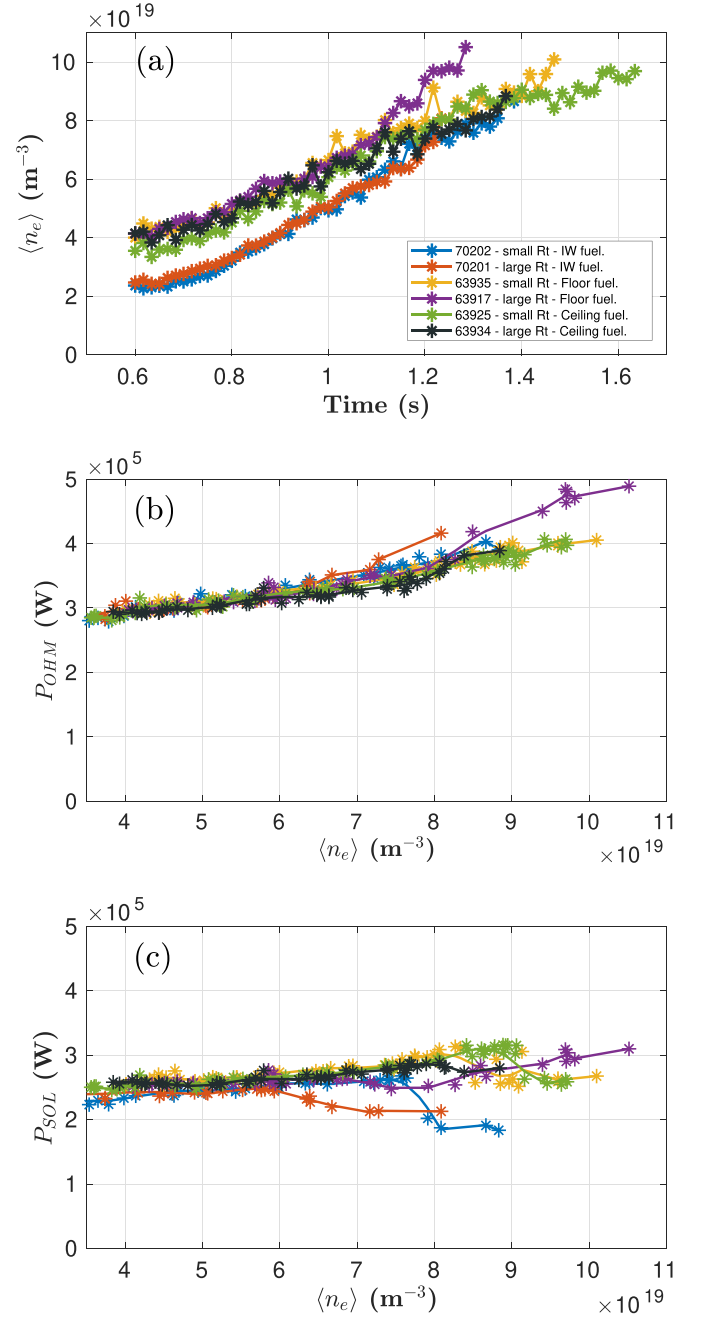


Figure 3. Density ramps at constant R_t —(a) line-averaged density $\langle n_e \rangle$ variation in time; (b) ohmic power P_{OHM} variation against $\langle n_e \rangle$; (c) power to the SOL P_{SOL} variation against $\langle n_e \rangle$.

gradually reduces. Using the CIII front as a proxy for the low temperature region in the divertor, the 2PM prediction on temperature is tested in these experiments.

The discharges have a similar time evolution for $\langle n_e \rangle$ and input ohmic power P_{OHM} dependence on $\langle n_e \rangle$, figures 3(a) and (b). An estimate of the power to the SOL, P_{SOL} , is obtained from the difference between P_{OHM} and the power radiated from the core, computed from bolometry, excluding a 5 cm circular region centered around the X-point, figure 4, as done

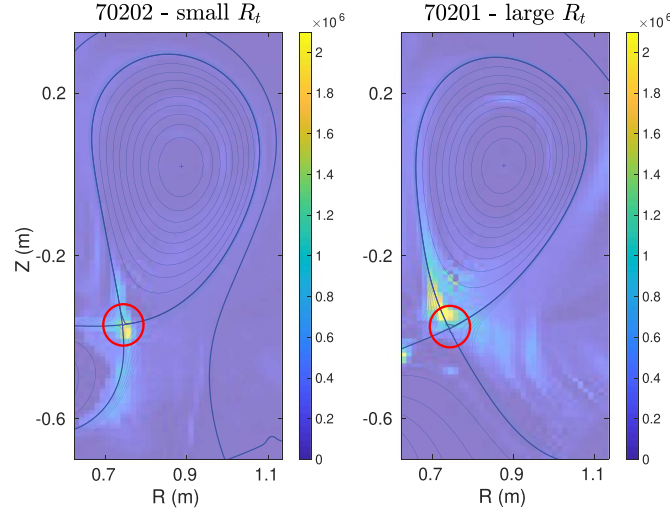


Figure 4. Density ramps at constant R_t , inner wall (IW) fuelling cases—Emissivity maps (W m^{-3}) at $\langle n_e \rangle = 6.75 \cdot 10^{19} \text{ m}^{-3}$. The colormap is saturated at $2.1 \cdot 10^6 \text{ W m}^{-3}$, to better highlight features of the emissivity maps away from the X-point. The red circle defines the 5 cm radial area centered around the X-point, excluded from core radiation computation.

Table 1. Density ramps at constant R_t —SOL geometry quantities at the OSP: inverse of the total magnetic field ($1/B_{\text{tot}}^{\text{OSP}} \propto R_t^{\text{OSP}}$, parallel OSP connection length $L_{\parallel}^{\text{OSP}}$ (measured from the OMP, 5 mm from the separatrix) and poloidal flux expansion $f_{x,\text{pol}}^{\text{OSP}}$ (measured at 5 mm from the separatrix).

Shot	R_t	Fuel.	$(1/B_{\text{tot}})^{\text{OSP}} (\text{T}^{-1})$	$L_{\parallel}^{\text{OSP}} (\text{m})$	$f_{x,\text{pol}}^{\text{OSP}}$
70202	Small	IW	0.50	14.2	2.79
70201	Large	IW	0.80	14.7	2.36
63935	Small	Floor	0.50	13.6	2.82
63917	Large	Floor	0.82	14.3	2.38
63925	Small	Ceiling	0.50	13.8	2.83
63934	Large	Ceiling	0.85	12.4	2.57

in [32]. The exclusion of this region leads to a more conservative, but more robust, evaluation of the power radiated from the core, avoiding mistakenly attributing radiation to the core region due to uncertainties in the bolometric reconstruction around the X-point. P_{SOL} dependence on $\langle n_e \rangle$ shows significant differences only in cases with IW fuelling (up to 25%), figure 3(c). Tomographic reconstruction of the emissivities for this fuelling location, figure 4, suggests that this difference can be ascribed to increased radiation inside the confined plasma region at higher $\langle n_e \rangle$. Thomson scattering measurements (not shown) also show that the density and temperature in the core and near the separatrix remain comparable in all cases. Relevant SOL geometry quantities are reported in table 1.

The dependence of the CIII front location along the outer leg, taken from inversions of MANTIS measurements, on $\langle n_e \rangle$ is analyzed to compare small and large R_t configurations, figure 5(a). Similar results are obtained by the DSS (not shown). However, variations in P_{SOL} and $L_{\parallel}^{\text{OSP}}$ can also influence the location of the CIII front, which is primarily determined by the temperature in the divertor leg. According to the 2PM, the OSP target temperature T_t (see (2), when changing the upstream control parameter from total pressure $p_{\text{tot},u}$ to density n_u [10, 18]) is

$$T_t^{2\text{PM}} \propto \frac{1}{R_t^2} \cdot \frac{q_{\parallel,u}^{10/7}}{n_u^2 L_{\parallel}^{4/7}}. \quad (24)$$

Assuming

$$n_u \propto \langle n_e \rangle \quad (25)$$

and using

$$q_{\parallel,u} \propto \frac{P_{\text{SOL}}}{\lambda_{\text{sol},u} 2\pi R_u B_{\text{pol},u} / B_{\text{tot},u}} \quad (26)$$

(24) becomes

$$T_t^{2\text{PM}} \propto \frac{1}{R_t^2} \cdot \frac{P_{\text{SOL}}^{10/7}}{\langle n_e \rangle^2 (L_{\parallel}^{\text{OSP}})^{4/7}}. \quad (27)$$

Note that this reasoning does not account for any difference in: I) the geometrical location and features of the upstream location (e.g. the scrape-off layer width $\lambda_{\text{sol},u}$); II) in-out power

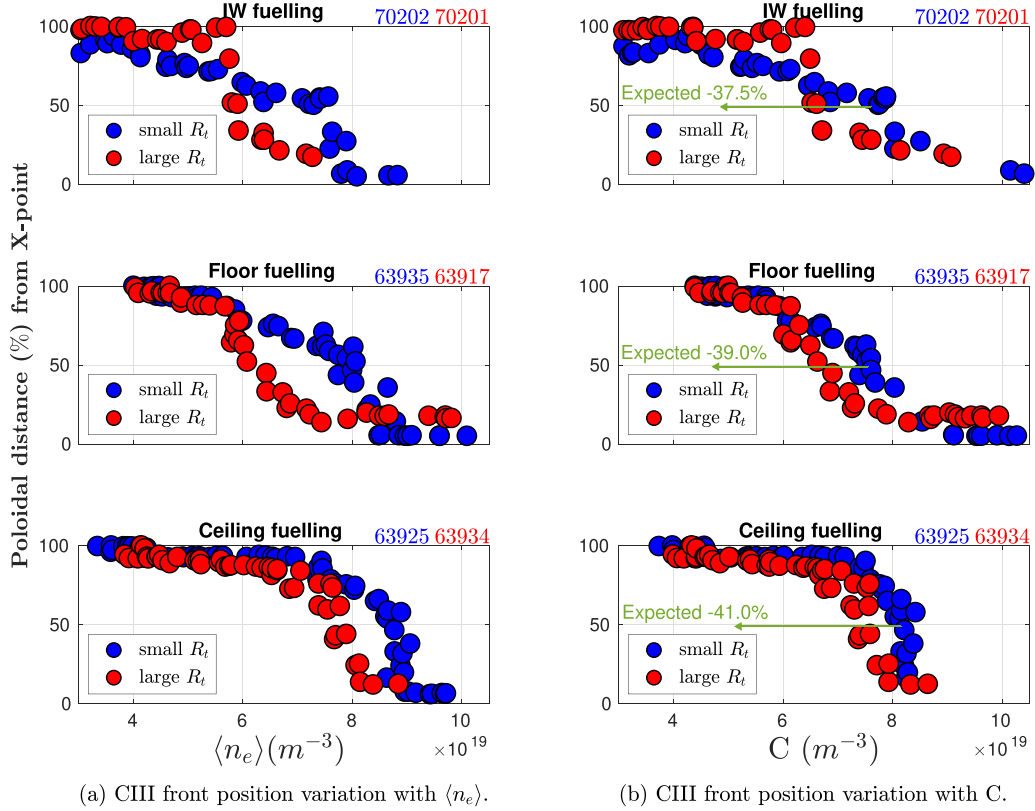


Figure 5. Density ramps at constant R_t —CIII front position analyses from MANTIS along the outer leg—CIII front position is defined in terms of relative (%) poloidal distance from the X-point, where 100% is the target position. The expected shifts of large R_t cases curves with respect to small R_t cases are also plotted, computed according to (29).

sharing³; III) the conducted-to-total power density ratio f_{cond} , or IV) the ratio $n_u/\langle n_e \rangle$.

From (27), the parameter

$$C \equiv \frac{\langle n_e \rangle \left(L_{\parallel}^{\text{OSP}} / L_{\parallel}^{\text{ref}} \right)^{2/7}}{\left(P_{\text{SOL}} / P_{\text{SOL}}^{\text{ref}} \right)^{5/7}} \quad (28)$$

can be defined as a *corrected* density. Representing the CIII front movement against C allows to consistently account for P_{SOL} and $L_{\parallel}^{\text{OSP}}$ variations between compared cases, according to the 2PM. Here, $L_{\parallel}^{\text{ref}} = 10\text{ m}$ and $P_{\text{SOL}}^{\text{ref}} = 2.5 \cdot 10^5\text{ W}$ are considered, figure 5(b). From (27), the large R_t configuration should see lower target temperatures for the same value of C . The CIII front movement from the target should thus happen at lower C values for the higher R_t cases. Given a specific front position obtained at values $C_{(\text{small } R_t)}$ in the small R_t cases, the expected reduced values for $C_{(\text{large } R_t)}^{\text{expected}}$ in the corresponding large R_t cases can be computed as

$$C_{(\text{large } R_t)}^{\text{expected}} = C_{(\text{small } R_t)} \cdot \frac{R_t^{(\text{small})}}{R_t^{(\text{large})}}. \quad (29)$$

³ Previous studies in TCV, in a similar scenario, suggest that the power redistribution between inner and outer target is not significantly affected by variations in R_t [7, 33].

For all the different fuelling cases, the variation in CIII front position with different R_t is much weaker than predicted by the 2PM, figure 5(b). While the CIII front position curves are predicted to shift at $\sim 40\%$ lower C values, passing from the small R_t to the large R_t configuration for all the cases, the experiments show this shift is always in between 10% and 20% lower C values.

3.3. R_t scans at constant density

Here the opposite scenario is investigated by poloidally sweeping the OSP at constant core density, from $R_t \simeq 0.7\text{ m}$ to 1.05 m , with both outward and inward sweeps. When R_t is modified, the target particle flux is also expected to vary according to the 2PM (see (4)). This prediction is tested in these experiments, using target LPs measurements.

During the strike-point sweeps, $\langle n_e \rangle$, P_{OHM} and P_{SOL} are kept approximately constant, figure 6, with an observed variation of up to 10%-20%. For all cases, $\langle n_e \rangle$ is always below $\sim 6.0 \cdot 10^{19}\text{ m}^{-3}$. At this density, for these experimental conditions, the CIII front in the outer leg remains close to the target and an attached state is maintained, as shown by the density ramps in 3.2, figure 5(a). Thomson scattering measurements (not shown) show that the density and the temperature in the core and near the separatrix remain comparable across

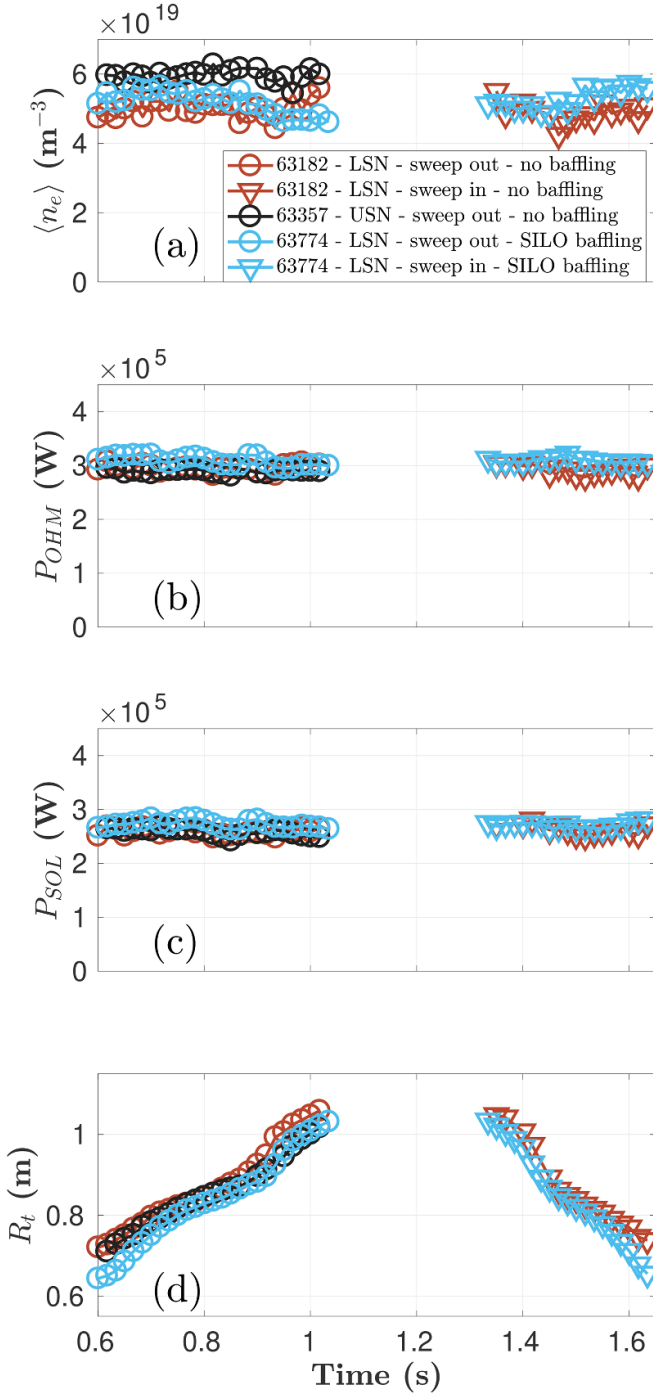


Figure 6. R_t sweeps at approximately constant line-averaged density $\langle n_e \rangle$ —(a) $\langle n_e \rangle$, (b) ohmic power P_{OHM} , (c) power to the SOL P_{SOL} and (d) OSP major radius R_t variations in time. In between ~ 1.05 and 1.35 s, the OSP is localized on a vessel segment for which a complete LPs coverage can not be achieved and, therefore, not of interest for the analyses and not reported here. For the USN case (black curve), only the outward sweep is available due to an early disruption.

the strike-point sweeps. The plasma geometry and the parallel OSP connection length L_{\parallel}^{OSP} (measured from the OMP, 5 mm from the separatrix) do not vary significantly during the sweeps, figure 7.

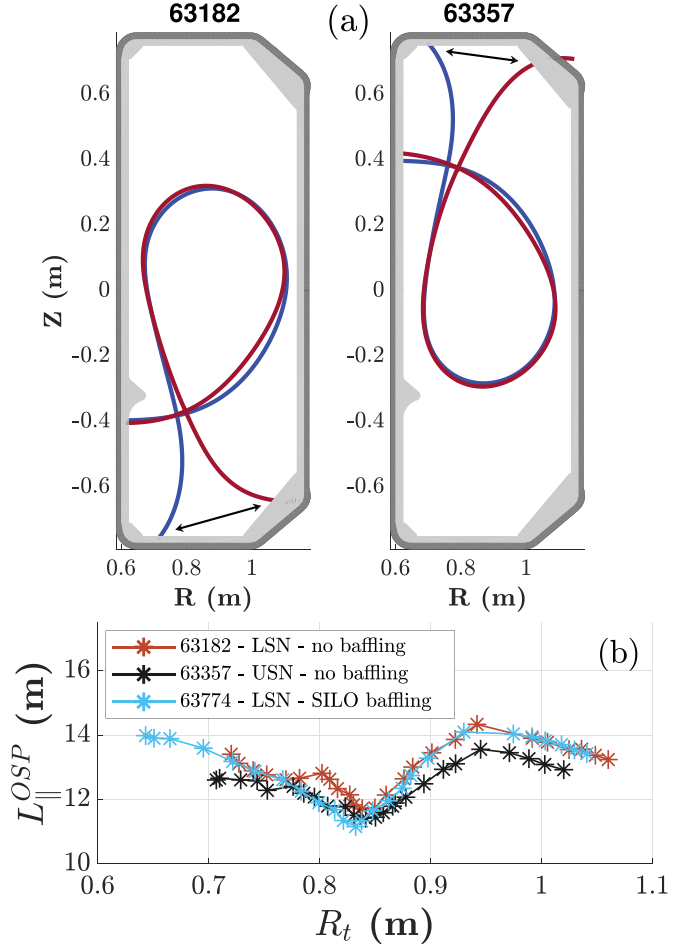


Figure 7. R_t sweeps at approximately constant line-averaged density $\langle n_e \rangle$ —(a) separatrix geometries for the un baffled cases, showing the minimum and maximum R_t achieved; (b) parallel connection length L_{\parallel}^{OSP} (taken at the outboard midplane, 5 mm from the separatrix) variation against R_t .

The dependence of the peak parallel particle flux density at the OSP Γ_t , taken from LP measurements, against R_t is analyzed, figure 8(a). However, variations in $\langle n_e \rangle$, P_{SOL} and L_{\parallel}^{OSP} can influence Γ_t variations. According to the 2PM the OSP peak parallel particle flux density Γ_t (see (4), when changing the upstream control parameter from total pressure $p_{tot,u}$ to density n_u [10, 18]) is proportional to

$$\Gamma_t^{2PM} \propto R_t \cdot \frac{n_u^2 L_{\parallel}^{4/7}}{q_{\parallel,u}^{3/7}} \propto R_t \cdot \frac{\langle n_e \rangle^2 (L_{\parallel}^{OSP})^{4/7}}{P_{SOL}^{3/7}}. \quad (30)$$

Here, the same approximations (see (25)) employed in section 3.2 are used. From (30), the variable

$$F \equiv \frac{\Gamma_t (P_{SOL}/P_{SOL}^{ref})^{3/7}}{(\langle n_e \rangle / \langle n_e \rangle^{ref})^2 (L_{\parallel}^{OSP} / L_{\parallel}^{ref})^{4/7}} \propto R_t \quad (31)$$

can be defined as a *corrected* parallel particle flux density. Representing F against R_t consistently accounts for $\langle n_e \rangle$,

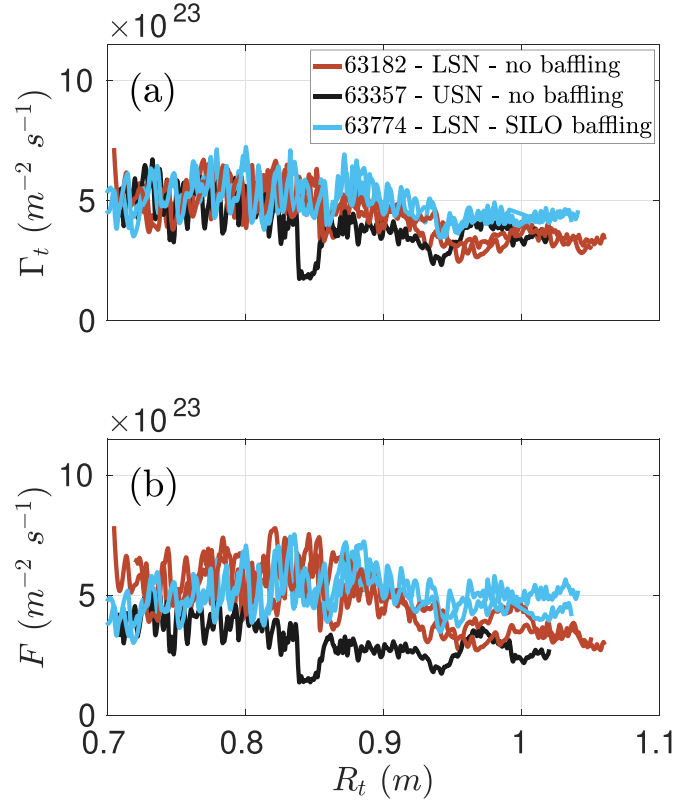


Figure 8. R_t sweeps at approximately constant line-averaged density $\langle n_e \rangle$ —peak parallel particle flux density Γ_t (a) and variable F (b) against R_t . For shots in the LSN configuration (cyan and brown lines), two lines are reported representing the two sweeps performed (outward and inward).

P_{SOL} and L_{\parallel}^{OSP} variations between compared cases, according to the 2PM. Here, $\langle n_e \rangle^{\text{ref}} = 5.5 \cdot 10^{19} \text{ m}^{-3}$, $L_{\parallel}^{\text{ref}} = 10 \text{ m}$ and $P_{SOL}^{\text{ref}} = 2.5 \cdot 10^5 \text{ W}$ are considered. From (31), F is expected to increase linearly with R_t , which is, however, not observed in the experiments, figure 8(b). For all the different cases, the variation of F with R_t is much weaker than predicted by the 2PM. Significant discrepancies from the 2PM predictions, consistent with this result, are also observed for the integrated particle flux (not shown).

4. Modeling of parallel flows in the divertor

Parallel flows can potentially explain part of the discrepancies between the 2PM predictions and the SXD experiments in TCV, sections 2.3 and 2.4. As a direct, reliable measurement of parallel flows was not available in the experiments, analytical and numerical modeling are presented in this section to assess if this effect can be significant in the experimental conditions.

4.1. Mach number evolution and possibility for supersonic flows

The impact of parallel flows on total flux expansion effects increases with higher values of the Mach number M in the divertor, causing an increase of M_{eff} , (14)–(16). The evolution

equation for M along a SOL flux tube is obtained by combining particle and momentum balances. For a single hydrogenic ion species ($n_e = n_i = n$)

$$(1 - M^2) \partial_s (M) = \frac{1 + M^2}{nc_s} S_{\text{par}} + \frac{M(1 + M^2)}{c_s} \partial_s (c_s) + A_{\perp} M \partial_s \left(\frac{1}{A_{\perp}} \right) - \frac{M}{m_i n c_s^2} S_{\text{mom}} \quad (32)$$

where s is a length coordinate along the flux tube, increasing from upstream to target ($s = s_t$), S_{par} and S_{mom} are effective sources/sinks in the flux tube for particles and momentum, respectively, related to volumetric sources and cross-field effects, see (8) and (9) and $c_s = \sqrt{(T_e + T_i)/m_i}$ is the local sound speed. The derivation of (32) is shown in appendix D. Note that (32) must satisfy the Bohm–Chodura condition [18], i.e. $M \geq 1$,⁴ at the target, as the target corresponds to the sheath entrance in this fluid model. Qualitatively, (32) shows that:

⁴ As explained in section 2.1, here the Mach number M is defined through the isothermal sound speed $c_s = \sqrt{(T_e + T_i)/m_i}$. However, the real sound speed at the divertor entrance, through which the Bohm–Chodura condition should be defined, is usually $c_s^{\text{real}} > c_s$ [34, 35]. This implies that at the target entrance it holds $M = v_{\parallel}/c_s > v_{\parallel}/c_s^{\text{real}} \geq 1$. In this sense, the analyses presented in this

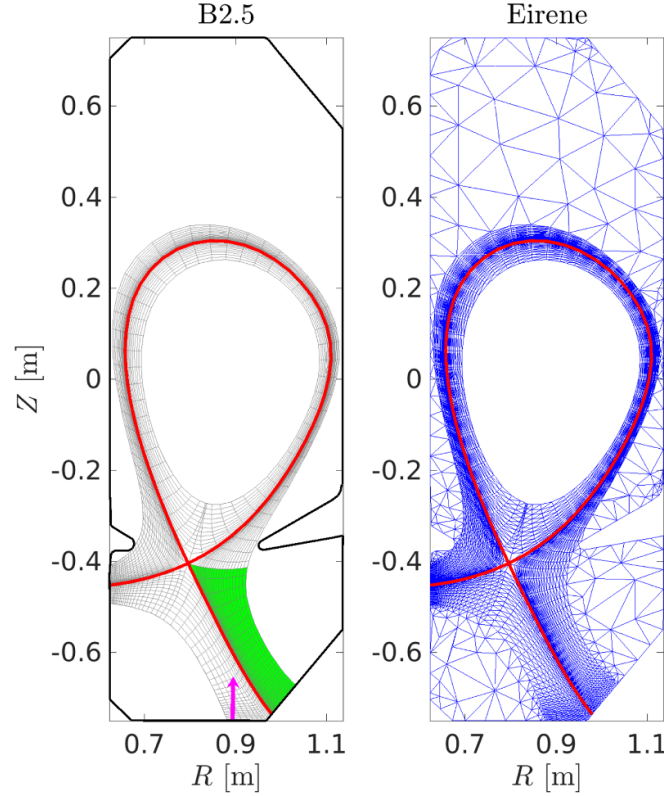


Figure 9. B2.5 and Eirene meshes for the SOLPS simulation. The pink arrow indicates the location for the fuelling. The green shaded area indicates the domain considered for the analyses of the outer leg.

- Four main drivers are responsible for M variation along a field line: particle and momentum effective sources/sinks (both volumetric sources and cross-field effects), sound speed c_s variation, and total flux expansion.
- The effect of these drivers is reversed when M is lower or higher than 1, i.e. whether the plasma flow is subsonic or supersonic.
- A necessary condition for a supersonic transition is a change of sign of the right-hand-side of (32).

Moreover, the constraint provided by the Bohm condition at the target allows to extract a sufficient (but not necessary) condition for the development of supersonic flows at the target. *If the right-hand-side of (32) is negative in a region in front of the target, then the flow must be supersonic.*

This case is interesting for the SXD configuration. Considering the ideal case where $S_{par,mom}$ and $\partial_s(c_s)$ are negligible in a region in front of the target, the right-hand-side of (32) is then negative in the same region in the outer leg, due to total flux expansion, and supersonic flows would arise. The idea that the convergent-divergent magnetic structure of a flux tube, such as in the outer leg of a SXD configuration, can favour supersonic flows at target has already been addressed

before [35–37] and demonstrated numerically [38, 39]. In consequence, M_{eff} and parallel flow effects on total flux expansion are suggested to be potentially significant for the SXD configuration.

Moreover, when the other drivers are considered, for low target temperature (i.e. $T_t \lesssim 5$ eV) as required in detached conditions, in front of the target:

- S_{par} is negative: at low temperatures the ionization front moves away from the target, and the only effective particle sources/sinks will be radial transport⁵ and recombination that both make S_{par} negative.
- $\partial_s(c_s)$ is negative.
- S_{mom} is negative due to charge exchange, recombination and radial transport (thus $-S_{mom}$ will be positive).

In the outer leg of the SXD configuration, 3 out of 4 terms on the right-hand-side of (32) are therefore negative. This type of analysis can be also applied to other divertor configurations, even with negligible total flux expansion, and supersonic flows can arise for similar target conditions [40–43]. However, different divertor conditions (e.g. a high-recycling regime, with

section is conservative, and a detailed analyses taking into account the *real* sound speed at the divertor entrance would imply even larger values of M_{eff} .

⁵ Here and in the following radial particle and momentum transport are considered negative contributions to S_{par} and S_{mom} . This is generally true for the hottest channels in the common flux region of the SOL.

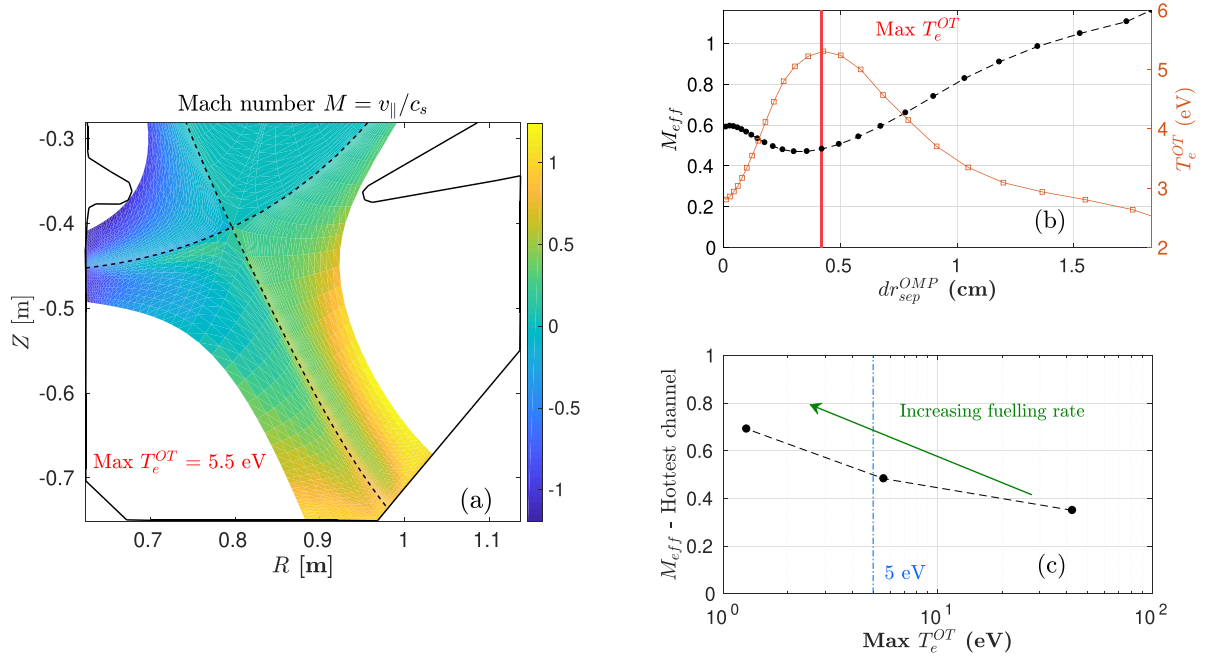


Figure 10. (a) Mach number $M = v_{\parallel}/c_s$ map in the divertor region, for the intermediate fuelling rate case, where v_{\parallel} is the parallel velocity of the main plasma species D^+ and c_s is the plasma sound speed, accounting for C impurities resulting from wall sputtering. (b) effective Mach number M_{eff} and outer target temperature T_e^{OT} for different flux tubes, in the case of intermediate fuelling rate, mapped against their radial distance from the separatrix at the OMP $dr_{\text{sep}}^{\text{OMP}}$. The flux tube with higher outer target temperature is indicated by the red vertical line. (c) effective Mach number M_{eff} for the flux tube with highest outer target temperature ($\simeq \text{Min } M_{\text{eff}}$), against $\text{Max } T_e^{OT}$.

the ionization front still at the target [36]), or momentum sinks (e.g. friction) are unfavorable for supersonic flows. Therefore, the prediction of the target Mach number requires detailed modeling for each specific case, and additional validation through experiments dedicated to flow measurements.

4.2. SOLPS-ITER modeling of SXD experiments in TCV

A SOLPS-ITER simulation of TCV is used to study the patterns of parallel flows and M_{eff} in the divertor region. SOLPS-ITER is a transport code that couples the B2.5 multi-fluid solver with the kinetic Monte Carlo model neutral code Eirene [17, 44]. The simulation discussed in this work was already presented in [45], where details of the simulation setup are reported. The simulation features a baffled LSN geometry, figure 9, with parameters typical of an ohmically-heated L-mode plasma in TCV, such as the experiments presented in section 3. Drift effects are not included in this work, so radial transport is purely anomalous and incorporated by artificial cross-field diffusion. The fuelling rate is varied to allow the analyses of different divertor conditions.

At the targets, a Dirichlet boundary condition satisfying the marginal Bohm criterion [46] is applied, i.e. the parallel ion velocity at the sheath entrance is forced to match the plasma sound velocity (accounting for carbon impurities resulting from wall sputtering). This means that a Mach number $M = 1$ at the target is imposed, excluding, *a priori*, supersonic flows at the target (see section 4.1). This implies that the following evaluation of M_{eff} is conservative: M_{eff} could potentially have higher values in reality.

To compute M_{eff} , the common flux region of the outer leg is considered in the simulation, taking as the upstream location the divertor entrance, figure 9. This is also a conservative choice: the value of M_{eff} usually has a minimum for a choice of upstream location that is close to the X-point (see appendix B).

For each flux tube in the analyzed domain, M_{eff} is evaluated according to (14)–(16). Its value varies both with the radial position of the flux tube, figure 10(b), and with divertor conditions, figure 10(c), as higher values are achieved for lower target temperatures. For intermediate and higher fuelling rates, where divertor conditions are similar to the experiments presented in section 3, $M_{\text{eff}} \geq 0.5$ for all the flux tubes. This SOLPS-ITER simulation therefore suggests that M_{eff} and parallel flow effects on total flux expansion are significant in these conditions, even with the conservative choices in the present analyses.

5. Conclusions

In this paper, the role of total flux expansion on the pressure balance, neglected in the 2PM, is made explicit, by including the effect of parallel flows. This effect is quantified by an effective Mach number M_{eff} , characteristic of each flux tube. Its introduction allows decoupling geometrical from cross-field and sources/sinks effects in the momentum loss factor $f_{\text{mom-loss}}$. As a result, 2PM target quantity expressions can be rewritten, revealing that their dependence on total flux expansion, through the ratio R_u/R_t , depends on M_{eff} . The total flux

expansion effects on target quantities are reduced with increasing M_{eff} and can even reverse for target density and target particle flux. These modifications are applied to the detachment model by Lipschultz *et al* [11], showing that the dependence of the detachment window on total flux expansion weakens with increasing M_{eff} . Physically, this is ascribed to a negative static pressure gradient being established towards the target due to total flux expansion.

Experiments on the SXD configuration were performed in the TCV tokamak, testing 2PM predictions. These are ohmically-heated L-mode discharges, with a SN configuration, $I_p \sim 250$ kA and ion ∇B drift directed away from the X-point. In core density ramps, featuring a baffled geometry and a range of fuelling locations, the CIII front movement in the outer leg, used as a proxy for the plasma temperature, shows variations with the OSP radius R_t but weaker than in the 2PM predictions, particularly when accounting for variations in P_{SOL} and L_{\parallel} . In OSP sweeps, with approximately constant core density, the peak particle flux density at the OSP remains independent of R_t variations, while the 2PM predicts a linear increase.

To understand whether parallel flow effects can be significant in the experiments presented in this work, in the absence of experimental parallel flow measurements, both analytical and numerical modeling are employed. It is shown that a SXD configuration, due to the convergent-divergent magnetic structure of flux tubes in the outer leg, favors the development of supersonic flows, and therefore larger values of M_{eff} . An analysis of a SOLPS-ITER simulation with a baffled LSN geometry in TCV, with parameters typical of an ohmically-heated L-mode plasma, shows that $M_{\text{eff}} \geq 0.5$ in the outer leg, for diverter conditions similar to those in the experiments, even when using conservative choices in its evaluation. While the impact of other effects (e.g. differences in power redistribution, or in losses due to radial field transport or atomic processes—for example, due to a different neutral compression [15, 16]) cannot be ruled out, the modelling then suggests that parallel flows, at least partially, explain the discrepancy between the 2PM predictions and experiments.

Acknowledgments

This work has been carried out within the framework of the EUROfusion Consortium, via the Euratom Research and Training Programme (Grant Agreement No. 101052200—EUROfusion) and funded by the Swiss State Secretariat for Education, Research and Innovation (SERI). Views and opinions expressed are however those of the author(s) only and do not necessarily reflect those of the European Union, the European Commission, or SERI. Neither the European Union nor the European Commission nor SERI can be held responsible for them. This work was supported in part by the Swiss National Science Foundation.

Appendix A. Derivation of 2PM expressions for target quantities

In this appendix the expressions (2)–(4) are derived. To simplify the final expressions with respect to those reported in [10], it is assumed:

- (S-I) only hydrogenic ion species (i.e. $n = n_e = n_i$) and no net current (i.e. $v_{\parallel} = v_{e,\parallel} = v_{i,\parallel}$).
- (S-II) thermal equilibration is achieved in the flux tube (i.e. $T = T_e = T_i$).

An additional general assumption is needed:

- (A-I) the target corresponds to the sheath entrance (i.e. $q_{\parallel,t} = \gamma n_t T_t M_t \sqrt{2T_t/m_i}$, where $M_t = v_{\parallel,t}/c_{s,t} = v_{\parallel,t}/\sqrt{2T_t/m_i}$ is the Mach number at the target and γ is the sheath heat transmission coefficient). Note that, by Bohm condition at the sheath entrance, $M_t \geq 1$ must hold.

Introducing the standard definitions of power and momentum loss factors (5) and (6) and using the above assumptions

$$(1 - f_{\text{cooling}}) q_{\parallel,u} R_u = \gamma n_t T_t M_t \sqrt{\frac{2T_t}{m_i}} R_t \quad (\text{A.1})$$

$$(1 - f_{\text{mom-loss}}) p_{\text{tot},u} = 2(1 + M_t^2) n_t T_t \quad (\text{A.2})$$

where the total pressure at the target $p_{\text{tot},t}$ was rewritten as $p_{\text{tot},t}^e + p_{\text{tot},t}^i = 2n_t T_t + m_i n_t v_{\parallel,t}^2 = 2(1 + M_t^2) n_t T_t$.

The factor $n_t T_t$ is isolated in (A.2) and substituted into (A.1), before isolating T_t to obtain

$$T_t = \frac{2m_i (1 + M_t^2)^2}{\gamma^2 M_t^2} \cdot \frac{q_{\parallel,u}^2}{p_{\text{tot},u}^2} \cdot \frac{(1 - f_{\text{cooling}})^2}{(1 - f_{\text{mom-loss}})^2} \cdot \left(\frac{R_u}{R_t}\right)^2 \quad (\text{A.3})$$

n_t is then obtained from (A.2) and (A.3)

$$n_t = \frac{\gamma^2 M_t^2}{4m_i (1 + M_t^2)^3} \cdot \frac{p_{\text{tot},u}^3}{q_{\parallel,u}^2} \cdot \frac{(1 - f_{\text{mom-loss}})^3}{(1 - f_{\text{cooling}})^2} \cdot \left(\frac{R_t}{R_u}\right)^2 \quad (\text{A.4})$$

Finally, Γ_t is obtained as $n_t v_{\parallel,t} = M_t n_t \sqrt{2T_t/m_i}$

$$\Gamma_t = \frac{\gamma M_t^2}{2m_i (1 + M_t^2)^2} \cdot \frac{p_{\text{tot},u}^2}{q_{\parallel,u}} \cdot \frac{(1 - f_{\text{mom-loss}})^2}{(1 - f_{\text{cooling}})} \cdot \left(\frac{R_t}{R_u}\right) \quad (\text{A.5})$$

Note that $\gamma = \gamma(M_t) \simeq 7.5 + M_t^2$ [18, 19]. These expressions recover (2)–(4) when $M_t = 1$, that is hypothesis (S-III) in section 2.1.

Appendix B. Further comments and insights on total flux expansion effects on momentum balance and on the effective Mach number M_{eff}

The synergy between parallel flows and total flux expansion on total pressure balance

A short insight on the physical intuition behind the synergy between parallel flows and total flux expansion is provided here, highlighting the difference with the power balance.

Contrary to the power balance expression (10), the total flux expansion effect $-R^{-1}\partial_s(R)$ on the local total pressure variation in (11) is weighted by $\kappa = m_i n v_{\parallel}^2 / p_{\text{tot}} = M^2 / (1 + M^2)$. As a consequence, the local flux expansion effect is re-scaled according to the local parallel flow conditions, in terms of M . In particular, for $M \ll 1$, total flux expansion effects can be neglected.

The physical intuition is that the only component of the total pressure that is subject to the effect of the locally varying cross-section in the flux tube is the dynamic pressure $m_i n v_{\parallel}^2$. This is because, in this work, the static pressure ($p = nT$) is considered isotropic⁶, while the dynamic pressure is anisotropic, with a preferential direction along the flux tube. Mathematically, this is reflected in (9) by the fact that dynamic pressure enters the balance via the divergence operator whilst the static pressure via the gradient operator.

Mathematical definition of M_{eff} , counter-intuitive values and its dependence on the upstream location

From (14)–(16), M_{eff} (or κ_{eff}) can be defined as: *the value of M (or κ) which, when constant from upstream to target, would provide the same total pressure variation $p_{\text{tot},t}/p_{\text{tot},u}$ due to total flux expansion.* Despite $\kappa = M^2 / (1 + M^2) \in [0, 1]$, from (14) it is clear that κ_{eff} can in principle take on any real value, due to the averaging process against $R^{-1}\partial_s(R)$. This reflects in $M_{\text{eff}} \rightarrow +\infty$ for $\kappa_{\text{eff}} \rightarrow 1^-$ or M_{eff} assuming imaginary values for $\kappa_{\text{eff}} \notin [0, 1]$ (see (16)). Despite being counter-intuitive, this does not pose a direct problem to the mathematical formulation: M_{eff} always enters the expressions presented in this work as $M_{\text{eff}}^2 / (1 + M_{\text{eff}}^2) = \kappa_{\text{eff}} \in \mathbb{R}$. For $\kappa_{\text{eff}} \rightarrow \pm\infty$, that can happen for $R_u \rightarrow R_t$, the indeterminate form $(R_u/R_t)^{\kappa_{\text{eff}}}$ appears in the expressions presented in this work. This is a consequence of forcing the geometrical term in the total pressure variation $(1 - f_{\text{mom-loss}})$ to take the form of a power of (R_u/R_t) (see (13)–(15)). However, this was necessary to maintain a simple form compatible with the algebraic expressions of the 2PM. However, as shown in the following examples, even when this happens the real physical parameter of interest, that is the geometrical term in the total pressure variation $(1 - f_{\text{mom-loss}})$, remains well defined.

Here, a pathological example is provided to discuss the meaning of infinite or imaginary values for M_{eff} , which could be difficult to understand in terms of the M_{eff} definition provided above. This also shows how the M_{eff} value depends on the upstream location. Consider a LSN geometry and focus

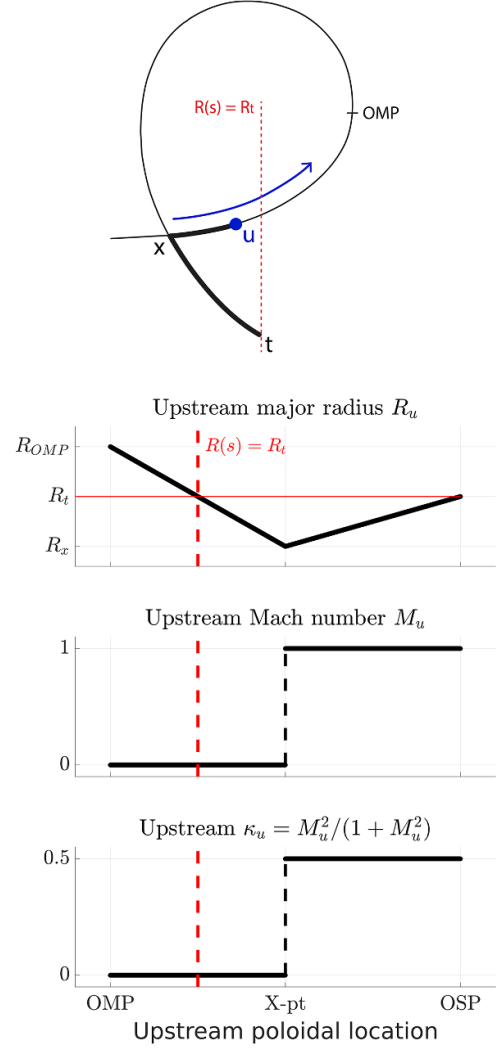


Figure B1. Graphical illustration of the example taken into consideration and variation of major radius R , Mach number M and $\kappa = M^2 / (1 + M^2)$ against upstream poloidal location. The vertical dotted red line indicates the location at which $R = R_t$, between OMP and X-point.

on computing M_{eff} for a flux tube in the outer divertor leg, varying the upstream location from the OSP to the OMP. A parallel length coordinate s is defined, increasing from $s = s_{\text{OMP}}$ at the OMP to $s = s_t$ at the OSP. Assume that:

- the Mach number is unitary between the X-point ($s = s_x$) and the OSP and null elsewhere, that is $M = \chi[s_x, s_t]$, where $\chi[s_1, s_2]$ is a function which equals 1 in between s_1 and s_2 and 0 elsewhere.
- $R_x < R_t < R_{\text{OMP}}$, where R is the major radius (R_x and R_{OMP} are the X-point and OMP major radii).

Figure B1 shows a graphical visualization of this example. Despite the R variation, the total pressure p_{tot} does not vary due to total flux expansion where $M = 0$, i.e. between the OMP and the X-point. p_{tot} then gradually decreases, due to total flux expansion, between the X-point and the OSP, as $M = 1$ and

⁶ This assumption may be questionable in some conditions, and the anisotropy of pressure, especially for ions, in parallel and radial directions might play a direct role on total flux expansion effects [39].

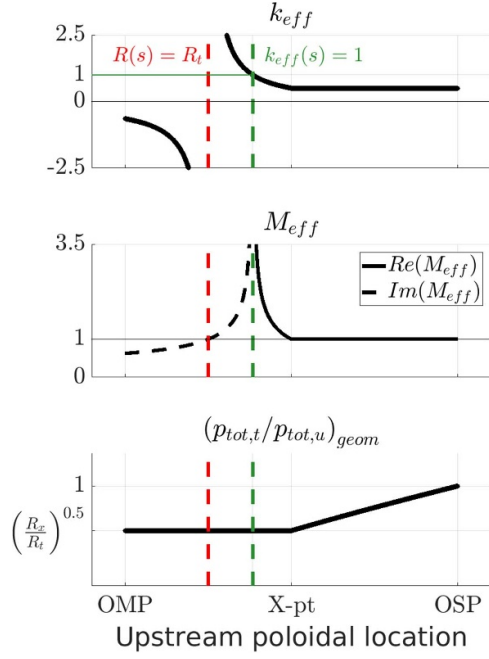


Figure B2. Variation of κ_{eff} , effective Mach number M_{eff} and geometrical factor in the total pressure variation $(p_{\text{tot},u}/p_{\text{tot},t})_{\text{geom}}$ against upstream poloidal location in the example taken into consideration. The vertical dotted red line indicates the location at which $R = R_t$, between OMP and X-point. The vertical green line indicates the location at which $\kappa_{\text{eff}} = 1$.

R increases (see (11)). In this simple case, κ_{eff} can be computed analytically for varying upstream location $s_u \in [s_{\text{OMP}}, s_t]$ by using (14)

$$\kappa_{\text{eff}} = 0.5 \cdot \frac{\ln(R_t/R_x)}{\ln(R_t/R_u)} \quad \text{for } s_u \in [s_{\text{OMP}}, s_x]$$

$$\kappa_{\text{eff}} = 0.5 \quad \text{for } s_u \in [s_x, s_t]$$

M_{eff} can be then computed by (16), together with the geometrical factor in the total pressure variation $p_{\text{tot},t}/p_{\text{tot},u}$ (see (15))

$$\begin{aligned} \left(\frac{p_{\text{tot},t}}{p_{\text{tot},u}}\right)_{\text{geom}} &= \left(\frac{R_u}{R_t}\right)^{0.5 \cdot \ln(R_t/R_x) / \ln(R_t/R_u)} \\ &= e^{-0.5 \cdot \ln(R_t/R_x)} \\ &= \left(\frac{R_x}{R_t}\right)^{0.5} \quad \text{for } s_u \in [s_{\text{OMP}}, s_x] \\ \left(\frac{p_{\text{tot},t}}{p_{\text{tot},u}}\right)_{\text{geom}} &= \left(\frac{R_u}{R_t}\right)^{0.5} \quad \text{for } s_u \in [s_x, s_t]. \end{aligned}$$

The results are represented in figure B2. For a choice of upstream location between the OSP and the X-point, where $M = 1$, M_{eff} and κ_{eff} are constants. The total pressure variation, due to total flux expansion, is reflected in the variation in $(p_{\text{tot},u}/p_{\text{tot},t})_{\text{geom}}$. When the upstream location is shifted beyond the X-point and towards the OMP, as the total pressure no longer varies due to total flux expansion, $(p_{\text{tot},u}/p_{\text{tot},t})_{\text{geom}}$ is constant. However, as (R_u/R_t) keeps varying in this region (in

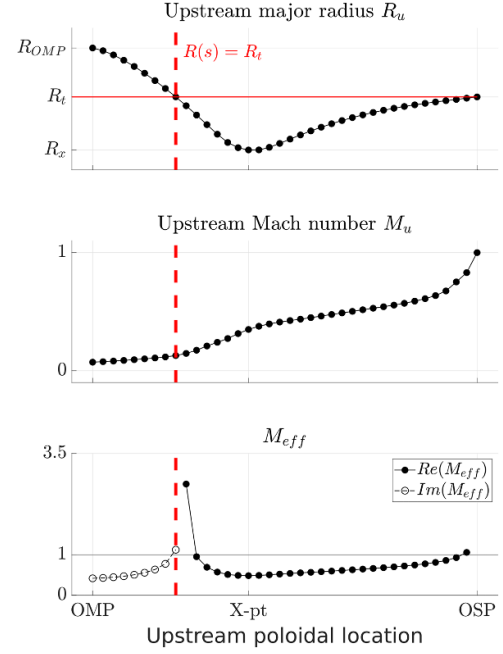


Figure B3. Variation of major radius R , Mach number M and effective Mach number M_{eff} against upstream poloidal location in the SOLPS-ITER simulations presented in section 4.2. The intermediate fuelling case and the flux tube with the highest target temperature are considered. The vertical dotted red line indicates the location at which $R = R_t$, between OMP and X-point.

this example, increasing towards the OMP), M_{eff} also varies to accommodate this change. When (R_u/R_t) increases above a given threshold (where $\kappa_{\text{eff}} = 1$), a positive M_{eff} can no longer accommodate this variation and imaginary values are obtained. This is understandable in terms of the definition provided above: taking for example the OMP as the upstream location, for which $R_u/R_t > 1$, there exists no constant value of $M \in \mathbb{R}$ which would result in a total pressure decrease towards the target, as in this example.

Similar results can be obtained in more realistic cases, such as for example the SOLPS-ITER simulation analyzed in section 4.2. Also in this case, flux tubes feature a convergent-divergent magnetic structure, between the OMP and the OSP, and a monotonically increasing M towards the OSP, figures 10(a) and B3. These conditions tend to push the minimum for M_{eff} close to the poloidal location where R is minimum, that is often the X-point location for the standard geometry of outer legs in diverted configurations, figure B3. This justifies why the choice of the divertor entrance, as the upstream location to evaluate M_{eff} in section 4.2, was termed as conservative.

Dependence of M_{eff} on the divertor leg geometry

M_{eff} is derived, through κ_{eff} , from a weighted average of $\kappa = M^2/(1 + M^2)$ along the flux tube, where the weighting factor is the local relative variation of the flux tube area $R^{-1} \partial_s(R)$ (see (14)–(16)). This implies that for a given M distribution, from upstream to target, the local flux expansion distribution along the leg influences the value of M_{eff} and, therefore, the magnitude by which total flux expansion effects are reflected

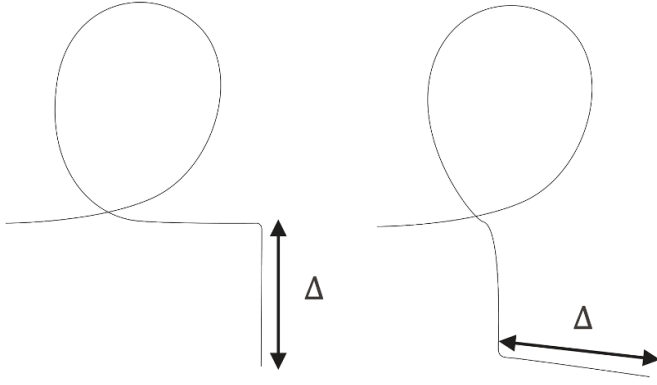


Figure B4. Graphical illustration of the two examples taken into consideration (case A on the left, case B on the right). Upstream location is here the X-point and the flux tube of interest is in the outer leg.

on total pressure variation, target quantities and detachment window. In other words, the divertor leg geometry influences the sensitivity to total flux expansion effects.

Here, a couple of pathological examples are provided to better highlight this point. Two cases, with the same total flux expansion R_t/R_u , are considered in which the local flux expansion is constant and focused only: (case A) in the region where $M = 0$; (case B) in the region where $M = 1$. Consider a SOL flux tube and a field aligned length coordinate $s = [0, L]$, where $s = 0$ corresponds to the upstream position (with major radius R_u) and $s = L$ corresponds to the target position (with major radius R_t). Assume the following profiles for the Mach number along the flux tube

$$M = 1 \cdot \chi [L - \Delta, L]$$

and for local relative flux expansion

$$\begin{aligned} \text{(case A)} \quad \frac{1}{R} \partial_s (R) &= \ln \frac{R_t}{R_u} \cdot \frac{\chi [0, L - \Delta]}{(L - \Delta)} \\ \text{(case B)} \quad \frac{1}{R} \partial_s (R) &= \ln \frac{R_t}{R_u} \cdot \frac{\chi [L - \Delta, L]}{\Delta} \end{aligned}$$

where $\Delta \in (0, L)$. In practice, it is imposed that M will increase instantaneously from 0 to 1 in the portion $[L - \Delta, L]$ of the flux tube in front of the target. Notice that in both cases the total flux expansion R_t/R_u is the same. Figure B4 shows a graphical visualization of these examples, for the outer leg of a single-null configurations (taking the X-point as upstream).

Computing now κ_{eff} by (14) and M_{eff} by (16), it is found

$$\begin{aligned} \text{(case A)} \quad \kappa_{\text{eff}} = 0 &\rightarrow M_{\text{eff}} = 0 \\ \text{(case B)} \quad \kappa_{\text{eff}} = 0.5 &\rightarrow M_{\text{eff}} = 1 \end{aligned}$$

It is then clear the drastic change in M_{eff} depending on the geometry of the flux tube, considering the same total flux expansion and flows pattern.

Appendix C. Derivation of detachment window expression

The derivation of (23) is presented. This is similar to the original derivation reported in [11]. In addition, the same hypothesis of thermal equilibration in the flux tube (i.e. $T = T_e = T_i$) is adopted, as in appendix A. Therefore, the plasma static pressure is $p = 2nT$.

Consider the total steady-state energy balance in a flux tube. Assume (a) cross-field transport effects are negligible. Assume also that (b) the ratio f_{cond} of conducted to total parallel power density is constant, and (c) Spitzer's formulation for parallel heat conductivity can be used: $K_{\parallel} = K_0 T^{5/2}$. The power balance is then

$$S_{\text{pwr}} = -\frac{1}{f_{\text{cond}}} B \partial_s \left(\frac{K_{\parallel}}{B} \partial_s (T) \right) \quad (\text{C.1})$$

where s is the length coordinate along a field line from target to upstream, here considered as corresponding to the X-point ($s : [0, s_x]$).

It is assumed that (d) $S_{\text{pwr}} = -n^2 f_t Q(T)$, which means the local effective power sources/sinks can be approximated with their only radiation-related component. Here n is the plasma density, f_t is the impurity fraction ($f_t = n_t/n$) and $Q(T)$ is a radiation efficiency function. The radiation efficiency $Q(T)$ is assumed (e) to be a function which peaks sharply just in a range $[T_c, T_h]$ (with $T_c < T_h$) and it is null outside of it.

The following change of variable is introduced

$$dz = \frac{B_x}{B} ds \quad (\text{C.2})$$

Practically, $z = \int_0^s dz' = \int_0^{s(z)} \frac{B_x}{B} ds'$ will be the volume ($ds/B \propto dV$) of the flux tube contained from the target ($s, z = 0$) up to the point of interest, normalized by a reference perpendicular area ($\propto 1/B_x$), where the upstream/X-point is taken as this reference.

Defining

$$K = K_{\parallel} \frac{B_x^2}{B^2} \quad (\text{C.3})$$

(C.1) becomes

$$\partial_z q = S_{\text{pwr}} \quad (\text{C.4})$$

with

$$q = -\frac{1}{f_{\text{cond}}} K \partial_z T \quad (\text{C.5})$$

$q = (1/f_{\text{cond}}) q_{\parallel, \text{cond}} B_x/B$ is then the total parallel power $Q_{\parallel} \propto (1/f_{\text{cond}}) q_{\parallel, \text{cond}}/B$ normalized by the same reference perpendicular area $\propto 1/B_x$.

Taking (C.4) and multiplying both sides by q , then integrating from $z(T_c)$ to $z(T_h)$ (note that $z(T_h) > z(T_c)$, in the chosen coordinate system)

$$[q^2]_{z(T_c)}^{z(T_h)} = - \int_{T_c}^{T_h} \frac{2}{f_{\text{cond}}} K(T) S_{\text{pwr}}(T) dT. \quad (\text{C.6})$$

Using assumptions (b) and (e), the square root of the integral on the right hand side of this equation becomes

$$\Delta q_{\text{rad}} \equiv \sqrt{\frac{2\kappa_0}{f_{\text{cond}}} \int_{T_c}^{T_h} \frac{B_x^2}{B^2} T^{5/2} n^2 f_l Q(T) dT}. \quad (\text{C.7})$$

Assume (f) the radiation region (i.e. the region in between $z(T_c)$ and $z(T_h)$) is so narrow that B and f_l variations are negligible in it. Assuming also that (g) volumetric processes and cross-field transport effects on momentum balance and total pressure redistribution are negligible in this region, this implies $p^2 = 4n^2 T^2 = p_{\text{tot}}^2 / (1 + M^2)^2$ can be taken out of the integral as its variation will be then linked just to total flux expansion effects (hence, B variation), negligible by assumption (f). Therefore

$$\Delta q_{\text{rad}} = \frac{B_x}{B_{z(T_h)}} p_{z(T_h)} \sqrt{\frac{K_0}{2f_{\text{cond}}}} f_l \mathcal{F} \quad (\text{C.8})$$

with $\mathcal{F} = \int_{T_c}^{T_h} \sqrt{T} Q(T) dT$.

The pressure at the detachment front entrance $p_{z(T_h)}$ is linked with pressure upstream/at the X-point p_u using (15), substituting $B \propto R^{-1}$. It is assumed that (h) volumetric processes and cross-field transport effects on momentum balance are negligible in the region between the X-point and the detachment front entrance. It then holds

$$\begin{aligned} \frac{p_{\text{tot},z(T_h)}}{p_{\text{tot},x}} &= \frac{1 + M_{z(T_h)}^2}{1 + M_x^2} \frac{p_{z(T_h)}}{p_u} = \\ &= \left(\frac{B_{z(T_h)}}{B_x} \right)^{\kappa_{\text{eff}}^{x \rightarrow z(T_h)}} \end{aligned} \quad (\text{C.9})$$

(C.8) becomes then

$$\begin{aligned} \Delta q_{\text{rad}} &= \frac{B_x}{B_{z(T_h)}} \frac{1 + M_x^2}{1 + M_{z(T_h)}^2} \\ &\cdot \left(\frac{B_{z(T_h)}}{B_x} \right)^{\kappa_{\text{eff}}^{x \rightarrow z(T_h)}} p_u \sqrt{\frac{K_0}{2f_{\text{cond}}}} f_l \mathcal{F} = \\ &= \frac{1 + M_x^2}{1 + M_{z(T_h)}^2} \left(\frac{B_x}{B_{z(T_h)}} \right)^{1 - \kappa_{\text{eff}}^{x \rightarrow z(T_h)}} \\ &\cdot p_u \sqrt{\frac{K_0}{2f_{\text{cond}}}} f_l \mathcal{F} \end{aligned} \quad (\text{C.10})$$

Finally, to obtain a model for the operational window for different control parameters, it is assumed that (i) the power leaving the cold detachment front is negligible. This will imply $q_{z(T_h)} = -\Delta q_{\text{rad}}$ by (C.6). The power entering the hot detachment front must then match the power entering upstream/at the X-point, thanks to assumption (d), and the latter can be expressed as $q_i = -P_{\text{SOL}}$, by definition of q .

Now one can equate $q_{z(T_h)}$ and q_i and solve in terms of the control parameters $\zeta = [p_u, f_l, P_{\text{SOL}}]$. The front position $z(T_h)$ is then set to be at the X-point first and then at the target to find the corresponding values $\zeta_{x,t}$ (leaving the others parameters

constant). Dividing these two values, the detachment window is obtained

$$\frac{\zeta_x}{\zeta_t} = \left(\left(\frac{B_{\text{tot},x}}{B_{\text{tot},t}} \right)^{1 - \kappa_{\text{eff}}} \frac{1 + M_x^2}{1 + M_t^2} \right)^\beta \quad (\text{C.11})$$

with $\beta = [1, 2, -1]$.

Appendix D. Derivation of mach number evolution equation

Consider the steady-state ion particle balance and plasma momentum balance along a flux tube

$$B \partial_s \left(\frac{nv_{\parallel}}{B} \right) = S_{\text{par}} \quad (\text{D.1})$$

$$B \partial_s \left(\frac{m_i n v_{\parallel}^2}{B} \right) = -\partial_s (nT^*) + S_{\text{mom}} \quad (\text{D.2})$$

where s is a length reference coordinate along the flux tube and $S_{\text{par}, \text{mom}}$ includes contributions from volumetric sources and cross-field transport effects. A single hydrogenic ion species and quasi-neutrality ($n_e = n_i = n$) are considered. For the sake of simplicity in the notation, $T^* = T_e + T_i$ is introduced.

Start rewriting the pressure term in (D.2)

$$\begin{aligned} B \partial_s \left(\frac{m_i n v_{\parallel}^2}{B} \right) &= -B \partial_s \left(\frac{nT^*}{B} \right) \\ &\quad - \frac{nT^*}{B} \partial_s (B) + S_{\text{mom}}. \end{aligned} \quad (\text{D.3})$$

In both (D.1) and (D.3), isolate $\partial_s(n)$

$$\partial_s(n) = \frac{S_{\text{par}}}{v_{\parallel}} - \frac{nB}{v_{\parallel}} \partial_s \left(\frac{v_{\parallel}}{B} \right) \quad (\text{D.4})$$

$$\begin{aligned} m_i v_{\parallel}^2 \partial_s(n) + nB \partial_s \left(\frac{m v_{\parallel}^2}{B} \right) &= -T^* \partial_s(n) \\ -nB \partial_s \left(\frac{T^*}{B} \right) - \frac{nT^*}{B} \partial_s(B) &+ S_{\text{mom}}. \end{aligned} \quad (\text{D.5})$$

Reordering and inserting (D.4) into (D.5)

$$\begin{aligned} -\frac{nB}{v_{\parallel}} (m_i v_{\parallel}^2 + T^*) \partial_s \left(\frac{v_{\parallel}}{B} \right) &+ (m_i v_{\parallel}^2 + T^*) \frac{S_{\text{par}}}{v_{\parallel}} \\ &= -nB \partial_s \left(\frac{m_i v_{\parallel}^2 + T^*}{B} \right) \\ &\quad - \frac{nT^*}{B} \partial_s(B) + S_{\text{mom}}. \end{aligned} \quad (\text{D.6})$$

Introducing $c_s = \sqrt{T^*/m_i}$ and reordering

$$\begin{aligned} -B (v_{\parallel}^2 + c_s^2) \partial_s \left(\frac{v_{\parallel}}{B} \right) &+ v_{\parallel} B \partial_s \left(\frac{v_{\parallel}^2 + c_s^2}{B} \right) = \\ &= - (v_{\parallel}^2 + c_s^2) \frac{S_{\text{par}}}{n} - v_{\parallel} \frac{c_s^2}{B} \partial_s(B) + \frac{v_{\parallel} S_{\text{mom}}}{m_i n}. \end{aligned} \quad (\text{D.7})$$

The left-hand-side of this equation is equivalent to

$$-\left(c_s^2 - v_{\parallel}^2\right) \partial_s (v_{\parallel}) + 2v_{\parallel} c_s \partial_s (c_s). \quad (\text{D.8})$$

Exploiting this and introducing $M = v_{\parallel}/c_s$, one obtains

$$\begin{aligned} \frac{1-M^2}{c_s} \partial_s (v_{\parallel}) &= 2 \frac{M}{c_s} \partial_s (c_s) \\ + (1+M^2) \frac{S_{par}}{nc_s} + \frac{M}{B} \partial_s (B) - \frac{MS_{mom}}{m_i nc_s^2} \end{aligned} \quad (\text{D.9})$$

which can be rewritten as

$$\partial_s (v_{\parallel}) = \partial_s (Mc_s) = M \partial_s (c_s) + c_s \partial_s (M). \quad (\text{D.10})$$

Exploiting this in (D.9) and using $B \propto (A_{\perp})^{-1}$, it is finally possible to retrieve (32)

$$\begin{aligned} (1-M^2) \partial_s (M) &= \frac{1+M^2}{nc_s} S_{par} \\ &+ \frac{M(1+M^2)}{c_s} \partial_s (c_s) \\ &+ A_{\perp} M \partial_s \left(\frac{1}{A_{\perp}} \right) \\ &- \frac{M}{m_i nc_s^2} S_{mom}. \end{aligned} \quad (\text{D.11})$$

ORCID iDs

M. Carpita  <https://orcid.org/0009-0006-3481-5197>
O. Février  <https://orcid.org/0000-0002-9290-7413>
H. Reimerdes  <https://orcid.org/0000-0002-9726-1519>
C. Theiler  <https://orcid.org/0000-0003-3926-1374>
D. Galassi  <https://orcid.org/0000-0003-3388-4538>
S. Gorno  <https://orcid.org/0000-0003-0524-7283>
A. Perek  <https://orcid.org/0000-0002-4117-0298>
G. Sun  <https://orcid.org/0000-0001-6761-6019>
E. Tonello  <https://orcid.org/0000-0001-8335-8873>
C. Wüthrich  <https://orcid.org/0000-0001-7548-2452>

References

- [1] Donne T. and Morris W. 2018 European research roadmap to the realisation of fusion energy (EUROfusion) (available at: https://euro-fusion.org/wp-content/uploads/2022/10/2018_Research_roadmap_long_version_01.pdf)
- [2] Wischmeier M. et al 2015 *J. Nucl. Mater.* **463** 22–29
- [3] Stangeby P.C. and Leonard A.W. 2011 *Nucl. Fusion* **51** 063001
- [4] Pitcher C.S. and Stangeby P.C. 1997 *Plasma Phys. Control. Fusion* **39** 779
- [5] Fenstermacher M.E. et al 1999 *Plasma Phys. Control. Fusion* **41** A345
- [6] Pitts R.A. et al 2019 *Nucl. Mater. Energy* **20** 100696
- [7] Theiler C. et al 2017 *Nucl. Fusion* **57** 072008
- [8] Reimerdes H. et al 2020 *Nucl. Fusion* **60** 066030
- [9] Valanju P.M., Kotschenreuther M., Mahajan S.M. and Canik J. 2009 *Phys. Plasmas* **16** 056110
- [10] Stangeby P.C. 2018 *Plasma Phys. Control. Fusion* **60** 044022
- [11] Lipschultz B., Parra F.I. and Hutchinson I.H. 2016 *Nucl. Fusion* **56** 056007
- [12] Petrie T.W. et al 2013 *Nucl. Fusion* **53** 113024
- [13] Reimerdes H. et al 2022 *Nucl. Fusion* **62** 042018
- [14] Moulton D., Harrison J., Lipschultz B. and Coster D. 2017 *Plasma Phys. Control. Fusion* **59** 065011
- [15] Fil A., Lipschultz B., Moulton D., Dudson B.D., Février O., Myatra O., Theiler C., Verhaegh K. and Wensing M. 2020 *Plasma Phys. Control. Fusion* **62** 035008
- [16] Meineri C., Muscente P., Theiler C. and Galassi D. 2023 *Nucl. Mater. Energy* **34** 101383
- [17] Wiesen S. et al 2015 *J. Nucl. Mater.* **463** 480–4
- [18] Stangeby P.C. 2000 *The Plasma Boundary of Magnetic Fusion Devices* (Institute of Physics Publishing)
- [19] Kotov V. and Reiter D. 2009 *Plasma Phys. Control. Fusion* **51** 115002
- [20] Cowley C., Lipschultz B., Moulton D. and Dudson B. 2022 *Nucl. Fusion* **62** 086046
- [21] Hofmann F. et al 1994 *Plasma Phys. Control. Fusion* **36** B277
- [22] Reimerdes H. et al 2021 *Nucl. Fusion* **61** 024002
- [23] Février O. et al 2021 *Nucl. Mater. Energy* **27** 100977
- [24] Hawke J. et al 2017 *J. Instrum.* **12** C12005
- [25] De Oliveira H., Marmillod P., Theiler C., Chavan R., Février O., Labit B., Lavanchy P., Marlétaz B. and Pitts R.A. 2019 *Rev. Sci. Instrum.* **90** 083502
- [26] Février O., Theiler C., De Oliveira H., Labit B., Fedorczak N. and Baillod A. 2018 *Rev. Sci. Instrum.* **89** 053502
- [27] Verhaegh K. et al 2017 *Nucl. Mater. Energy* **12** 1112–7
- [28] Perek A. et al 2019 *Rev. Sci. Instrum.* **90** 123514
- [29] Harrison J. et al 2017 *Nucl. Mater. Energy* **12** 1071–6
- [30] Sheikh U.A., Simons L., Duval B.P., Février O., Moret D., Allegrucci A., Bernert M., Crisinel F., Tersztyánszky T. and Villinger O. 2022 *Rev. Sci. Instrum.* **93** 113513
- [31] Moret J.-M., Duval B.P., Le H.B., Coda S., Felici F. and Reimerdes H. 2015 *Fusion Eng. Des.* **91** 1–15
- [32] Février O. et al 2020 *Plasma Phys. Control. Fusion* **62** 035017
- [33] Maurizio R. 2020 Investigating Scrape-Off Layer transport in alternative divertor geometries on the TCV tokamak *PhD Thesis EPFL* (<https://doi.org/10.5075/epfl-thesis-9893>)
- [34] Munsch Y. et al 2023 *HAL Open Science* (available at: <https://hal.science/hal-04122266/document>)
- [35] Riemann K. 1995 *IEEE Trans. Plasma Sci.* **23** 709–16
- [36] Bufferand H., Ciraolo G., Dif-Pradalier G., Ghendrih P., Tamain P., Marandet Y. and Serre E. 2014 *Plasma Phys. Control. Fusion* **56** 122001
- [37] Inutake M., Ando A., Hattori K., Tobari H. and Yagai T. 2002 *J. Plasma Fusion Res.* **78** 1352–60
- [38] Togo S., Takizuka T., Reiser D., Sakamoto M., Ogawa Y., Ezumi N., Ibano K., Nojiri K., Li Y. and Nakashima Y. 2019 *Nucl. Mater. Energy* **19** 149–54
- [39] Togo S., Takizuka T., Reiser D., Sakamoto M., Ezumi N., Ogawa Y., Nojiri K., Ibano K., Li Y. and Nakashima Y. 2019 *Nucl. Fusion* **59** 076041
- [40] Marchuk O., Tokar M.Z. 2008 *Contrib. Plasma Phys.* **48** 164–8
- [41] Takizuka T. et al 2001 *J. Nucl. Mater.* **290–293** 753–6
- [42] Ghendrih P. et al 2011 *Plasma Phys. Control. Fusion* **53** 054019
- [43] Stangeby P.C. 1991 *Plasma Phys. Control. Fusion* **33** 677
- [44] Xavier B., Dekeyser W., Pitts R., Coster D., Voskoboinikov S. and Wiesen S. 2016 *Plasma Fusion Res.* **11** 1403102
- [45] Wensing M. et al 2019 *Plasma Phys. Control. Fusion* **61** 085029
- [46] Bohm D. 1949 *The Characteristics of Electrical Discharges in Magnetic Fields* (McGraw-Hill)